

Impact of A-Site Cation Modification on Charge Transport Properties of Lead Halide Perovskite for Photovoltaics Applications

Quanyao Lin, Satyaprasad P Senanayak, Narges Yaghoobi Nia, Mejd Alsari, Samuele Lilliu, and Mojtaba Abdi-Jalebi*

Perovskite solar cells (PSCs) have reached a formidable power conversion efficiency of 25.7% over the years of development. One of the strategies that has been responsible for the development of stable and highly efficient PSCs is modifications of the monovalent A-site cations (methylammonium, MA; formamidinium, FA; cesium, Cs, etc.) in lead halide perovskites. Herein, the impact of modifying the monovalent cation (MA, FAMA, CsFAMA, potassium-passivated CsFAMA, rubidium-passivated CsFAMA) in lead halide perovskite on their optoelectronic, charge transport, and photovoltaic behavior is systematically studied. Reduced trap density and improved charge carrier mobility after introduction of FA and Cs in the $\text{MAPb}(\text{I}_{0.85}\text{Br}_{0.15})_3$ system are confirmed. Further passivation of the triple-cation perovskite with K and Rb enhances the optoelectronic characteristics, charge transport, and charge extraction efficiency in halide perovskite solar cells.

1. Introduction

Lead halide perovskite solar cells (PSCs) have reached an astonishing power conversion efficiency (PCE) of 25.7%,^[1] which has made them a viable contender for traditional silicon-based solar cells, mainly due to their superior optoelectronic properties, such as strong light absorption,^[2] long carrier lifetime,^[3] bandgap tunability,^[4] and low-temperature solution processability,^[5] enabling opportunity for cheap mass production of perovskite devices. The general formula for perovskite-based materials is ABX_3 , where the A sites are occupied by monovalent cation/s (e.g., methylammonium [MA]; formamidinium [FA]; cesium [Cs]), a divalent metal cation at B sites

(mostly Pb, also Sn), and one or more halides (e.g., I, Br, Cl) at X sites. Since the emergence of methylammonium lead halide (MAPbI_3) in 2009,^[6] monovalent cation engineering has been one of the key drivers for the steep rise in the device efficiency.

Despite the rapid progress of MAPbI_3 -based PSCs, its efficiency bottlenecks at around 20%^[7,8] due to its nonideal bandgap energy ($E_g = 1.52$ eV compared to $E_g = 1.40$ eV at AM1.5 solar spectrum for single-junction solar cells) as well as thermal and moisture instability.^[9,10] Formamidinium lead iodide (FAPbI_3) offers a decreased optical bandgap at 1.45 eV, while its photoactive phase (α -phase) is not thermodynamically stable at room temperature.^[11] To fix the problems possessed by these single-cation (SC) perovskite materials, double-cation (DC) perovskites, often a mixture of FA/MA, offer to adjust the bandgap for wider absorption spectra with improved thermal and structural stability. However, the formation of yellow nonperovskite phase is difficult to be eliminated unless a small quantity of Cs is further added to the FA/MA mixture.^[12] Thus far, triple-cation (TC) perovskites (CsFAMA), together with a mixture of iodide and bromide, have been the workhorse for highly stable and efficient PSCs with highly reproducible efficiencies above 23%.^[13] More recently, rubidium (Rb) and potassium (K) have shown great promise to be effective passivation agents for TC perovskites, showing superior optoelectronic properties and device performances.^[14,15]

Apart from the influence on the stability and bandgap of the resulting composition, monovalent cations also play significant roles in the carrier dynamics^[16,17] and ion migration^[14,18,19] in


Q. Lin, M. Abdi-Jalebi
Institute for Materials Discovery
University College London
Malet Place, London WC1E 7JE, UK
E-mail: m.jalebi@ucl.ac.uk

S. P. Senanayak
Nanoelectronics and Device Physics Lab
School of Physical Sciences
National Institute of Science Education and Research
OCC of HBNI, Jatni 752050, India

N. Yaghoobi Nia
School of Aerospace Engineering
University of Rome Sapienza
00138 Rome, Italy

M. Alsari
Department of Applied Physics and Astronomy
University of Sharjah
P. O. Box 27272, Sharjah, United Arab Emirates

S. Lilliu
Bullaki Ltd.
Covent Garden, London WC2H 9JQ, UK

 The ORCID identification number(s) for the author(s) of this article can be found under <https://doi.org/10.1002/ente.202300358>.

© 2023 The Authors. Energy Technology published by Wiley-VCH GmbH. This is an open access article under the terms of the Creative Commons Attribution License, which permits use, distribution and reproduction in any medium, provided the original work is properly cited.

DOI: 10.1002/ente.202300358

halide perovskite. For example, mixing FA, Cs, and/or Rb/K has been widely reported to significantly improve the lifetime of minority carriers by passivating the trap states.^[12,16,19,20] In addition, partial A-site substitution of different sizes can also strongly suppress ion migration by creating local distortion in crystal lattice and increasing its activation energy for migration.^[18,21]

In this work, we offer a systematic study on the impact of chemical modifications at the A-site cation as well as addition of monovalent cation passivation agents on the optoelectronic, charge transport, and photovoltaics behavior of perovskite. To do this, we use the same B-site cation (i.e., Pb) and mixed X-site halide (e.g., $I_{0.85}Br_{0.15}$) for a range of very well-known mixed cation compositions. The series include $MAPb(I_{0.85}Br_{0.15})_3$ (SC), $FA_{0.85}MA_{0.15}Pb(I_{0.85}Br_{0.15})_3$ (DC), and $Cs_{0.05}FA_{0.80}MA_{0.15}Pb(I_{0.85}Br_{0.15})_3$ (TC) as well as Rb-passivated TC (Rb-TC) and K-passivated TC (K-TC). Photothermal deflection spectroscopy (PDS), time-resolved photoluminescence spectroscopy (TRPL), photoluminescence quantum efficiency (PLQE) measurements, space-charge limited current (SCLC) measurements, and electrochemical impedance spectroscopy (EIS) have been carried out for each perovskite composition and correlated with the photovoltaic performances of their corresponding devices.

2. Results and Discussion

The absorption spectra measured by the PDS measurements exhibit a slight redshift when the dominant A-site cation becomes FA compared to pure MA (Figure 1a). Importantly, the subbandgap absorption slightly reduces from SC to DC

($\approx 10^{-4}$) and then significantly drops for TC and passivated TC perovskites to around 10^{-5} , indicating significantly reduced trap states in the films upon introduction of multicationic mixture into the perovskite composition. Indeed, the calculated Urbach energy (E_u), which is a measure of electronic disorder in a semiconductor, forms a tail in the PDS measurements. The Urbach energy (E_u) was observed to be extremely low for TC, Rb-TC, and K-TC (≈ 13 – 14 meV), indicating the lowest disorder, which translated into the enhanced semiconductor quality of these perovskite compositions (Figure 1b). Correspondingly, the TRPL experiments show a slight enhancement in the charge carrier lifetime for the FA/MA DC perovskite compared to the SC one from 61.8 to 77.1 ns (Figure 1c). The carrier lifetime further improves significantly for the TC sample to 196.9 ns and reaches the longest lifetime for the passivated TC perovskites (328.3 ns for Rb-TC and 364.4 ns for K-TC). The reason behind this significant increased carrier lifetime after cesium addition can be attributed to the increased crystallinity, which was proved by the larger grain sizes for TC-based perovskite films compared to SC in scanning electron microscopy (SEM) (Figure S1, Supporting Information), the elimination of PbI_2 peak after addition of Cs (Figure S2a, Supporting Information) in X-ray diffraction (XRD), and a strong increase at intermediate orientations in the synchrotron Grazing-incidence wide-angle X-ray scattering (GI-WAXS) diffraction patterns (Figure S2b, Supporting Information). This increased crystallinity therefore reduces defect states in the bulk for TC and results in a prolonged carrier lifetime.^[12,16,20] It has also been reported that cation mixing also causes broken symmetry in ground-state charge density and the induced polarizabilities enhances the excited carrier lifetime.^[22] In Figure S3, Supporting Information, we also show the TRPL of these perovskites measured at different fluences.

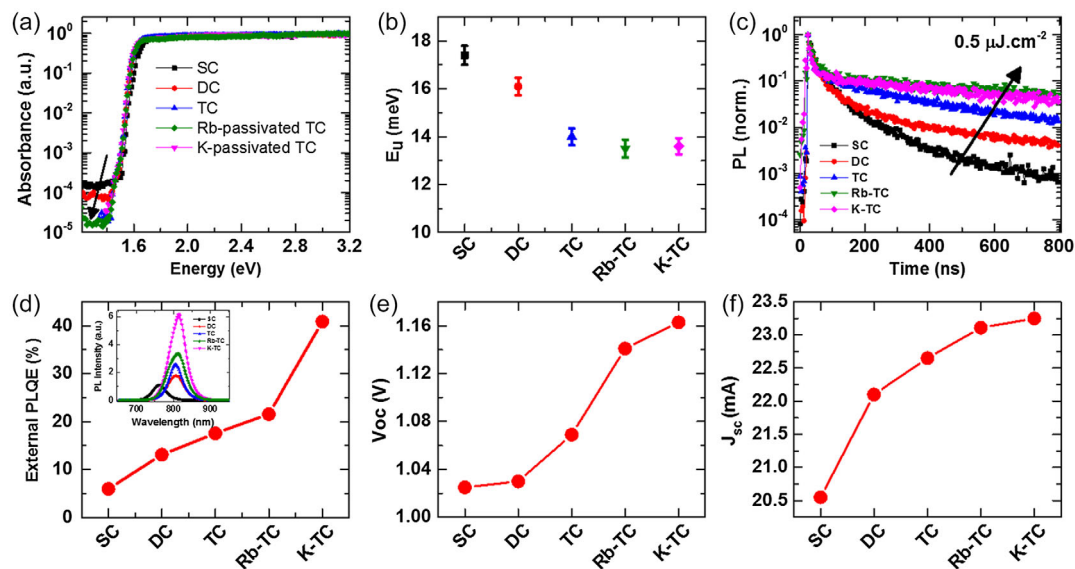


Figure 1. Optoelectronic characterization of multiple cation and passivated perovskite thin films. a) The absorption spectra, b) Urbach energy (E_u) for perovskite thin films ($MAPb(I_{0.85}Br_{0.15})_3$ (SC), $FA_{0.85}MA_{0.15}Pb(I_{0.85}Br_{0.15})_3$ (DC), $Cs_{0.05}FA_{0.80}MA_{0.15}Pb(I_{0.85}Br_{0.15})_3$ (TC), and 5% K- or 5% Rb-passivated TC) measured by photothermal deflection spectroscopy. c) TRPL decays of the perovskites with excitation at 400 nm and a pulse fluence of $0.5 \mu J cm^{-2}$ (excitation density of approximately $10^{16} cm^{-3}$). d) PLQE of perovskite thin films measured under illumination with a 532 nm laser at an excitation intensity equivalent to approximately 1 sun ($60 mW cm^{-2}$) after 600 s of illumination. e) Open-circuit voltage (V_{oc}) and f) short-circuit current (J_{sc}) as a function of perovskite composition.

We then plotted the setup-limited (time resolution about 1.5 ns), initial PL signal, PL_0 , for pulsed optical excitation (Figure S3f, Supporting Information). The transient PL measures the radiative component of the recombination rate

$$PL(t) \approx \frac{dn}{dt_{\text{rad}}}(t) \quad (1)$$

where n is the charge carrier density.^[23] We find that the initial PL signal scales quadratically with pump power and thus carrier density for all the different compositions, indicating a bimolecular recombination process for all the investigated charge carrier densities, as discussed previously in the literature.^[23]

In Figure 1d, we show the external PL quantum efficiency (PLQE) of the perovskite thin films with different cations and passivation agents measured at excitation densities equivalent to solar illumination conditions. We observe a significant increase in PLQE from 6% for SC to 13% for DC followed by further enhancement to 18% for TC and 22% for Rb-TC and reach a remarkable value of 41% for K-TC, further showing clear evidence that both Rb and K exhibit excellent passivation ability for TC perovskites. The corresponding PL spectrum for each of the perovskite compositions is shown in the inset of Figure 1d. Note that the major shift of PL peak from SC (761 nm) to DC (807 nm) is due to the substitution of larger sized FA compared to MA, leading to higher symmetry of cubic phase and a reduced bandgap.^[24] No obvious peak shift was observed after the inclusion of Cs, but further addition of both K and Rb caused a slight redshift to 815 nm due to the excess iodide content introduced by KI or RbI, respectively.^[19]

To validate how these optical characterization results translate to device performance, we also show the photovoltaic characterization of the perovskite solar cells using the device architecture FTO/c-TiO₂/mp-TiO₂/perovskite/Spiro-OMeTAD/Au. The J - V curves of the devices and the relative photovoltaic parameters are shown in Figure S4 and Table S1, Supporting Information. As expected from the relationship between luminescence and open-circuit voltage,^[25] the changes in V_{oc} of the devices closely follow the PLQE trends. From the J - V characteristic of the devices under dark conditions, the dark current onset of perovskite solar cells also validates the V_{oc} trend. Furthermore, we see an increase in J_{sc} from SC, DC to TC (Figure 1f), peaking for the passivated TC perovskites with Rb and K. This is expected from their substantially longer charge carrier lifetime from TRPL measurements because longer carrier lifetime typically leads to higher rate of charge extraction. We also reach higher values for fill factor of the solar cells with K- and Rb-passivated TC (Table S1, Supporting Information), suggesting suppression of Shockley–Reed–Hall type trap-assisted recombination due to the passivation effect particularly from K and Rb monovalent cations at the grain boundaries and interfaces.^[19,26] Finally, the enhanced photovoltaic parameters for the passivated perovskite films reflected in the PCE of the devices reaching more than 20% for K- and Rb-passivated TC comparing to 15% for SC, 17% for DC, and 18% for TC-based perovskite solar cells.

To understand the observed enhancement in charge transport properties with the substitution of multicationic mixtures and passivation, SCLC measurement was performed in a vertical device geometry for electron-only devices (FTO/TiO₂/

perovskite/PCBM/Al) and hole-only devices (ITO/PEDOT:PSS/perovskite/Au) with the same perovskite thickness and the charge carrier mobility (μ_{SCL}) was estimated using the Mott–Gurney law given by $J = \frac{9}{8} \epsilon_0 \epsilon_r \mu_{\text{SCL}} \frac{V^2}{d^3}$, where J is the current density, V is the potential applied, ϵ_0 is the vacuum permittivity, ϵ_r is the dielectric constant of the active material, and d is the thickness of the active layer measured by a stylus profilometer.

Typical I - V characteristics of different perovskite materials are shown in Figure 2a,b. Interestingly, it was possible to observe a trap-free space charge limited regime within <2 V range, indicating lower degree of disorder in these materials. Devices fabricated from MA SC perovskites exhibited electron mobility μ_e of 0.05 cm² V⁻¹ s⁻¹, in agreement with previous reports,^[27] and increases to 0.07 and 0.12 cm² V⁻¹ s⁻¹ for DC and Cs-based TC perovskites. The bulk electron mobility further improves to 0.15 and 0.3 cm² V⁻¹ s⁻¹ upon Rb and K passivation of the TC perovskites, respectively. Similar enhancement was also observed in the case of hole only devices and hole mobility μ_h of up to a maximum of 0.08 cm² V⁻¹ s⁻¹ was observed for K-passivated TC perovskite devices.

To further understand the reason for the increased μ_e and μ_h after cation mixing, temperature-dependent charge transport measurements were performed on these vertical devices over a temperature range of 100–300 K. The activation energy obtained from Arrhenius fits decreases from 153 meV for MAPb(I_{0.85}Br_{0.15})₃ devices to 77 meV for K-passivated TC perovskite, further proving less disorder for K-passivated perovskites. Similar enhancement is also observed in the hole activation energy which decreases from 167 to 103 meV for MAPb(I_{0.85}Br_{0.15})₃ to K-passivated TC perovskites, respectively. From these measurements we observe a clear trend, indicating that the Cs-based TC perovskite outperforms SC perovskite film in carrier charge transport facilitated by a decrease in the energy barrier for both electron and hole transport. The charge carrier mobility and the associated activation energy can be further enhanced with Rb and/or K passivation. The higher carrier mobility of films based on TC (pristine TC, Rb- and K-passivated TC) has also been reported to contribute on the higher J_{sc} and FF in the corresponding devices,^[16,19] as observed in our results.

We also performed detailed electrochemical impedance spectroscopy measurements on completed photovoltaic devices operating under illumination and open circuit conditions. The impedance measurement was performed by applying a small AC voltage of 50 mV while the frequency is swept from 100 Hz to 10 MHz. Electrochemical impedance spectroscopy (EIS) results are presented as a Nyquist plot, consisting of the real component of the impedance (Z') as X-axis and the imaginary part (Z'') as the ordinate. In the Nyquist plot, the low/intermediate frequency feature corresponds to charge accumulation at the interfaces which is generally characterized by the capacitance at the contacts (referred as C_{cont}) and Debye dielectric relaxation as well as the high-frequency component attributed to the transport of charge carriers. The data are then fitted with an equivalent circuit which consists of a series and parallel network of RC circuits, indicating the different resistive and capacitive components of a perovskite photovoltaic cell (Figure S5b,

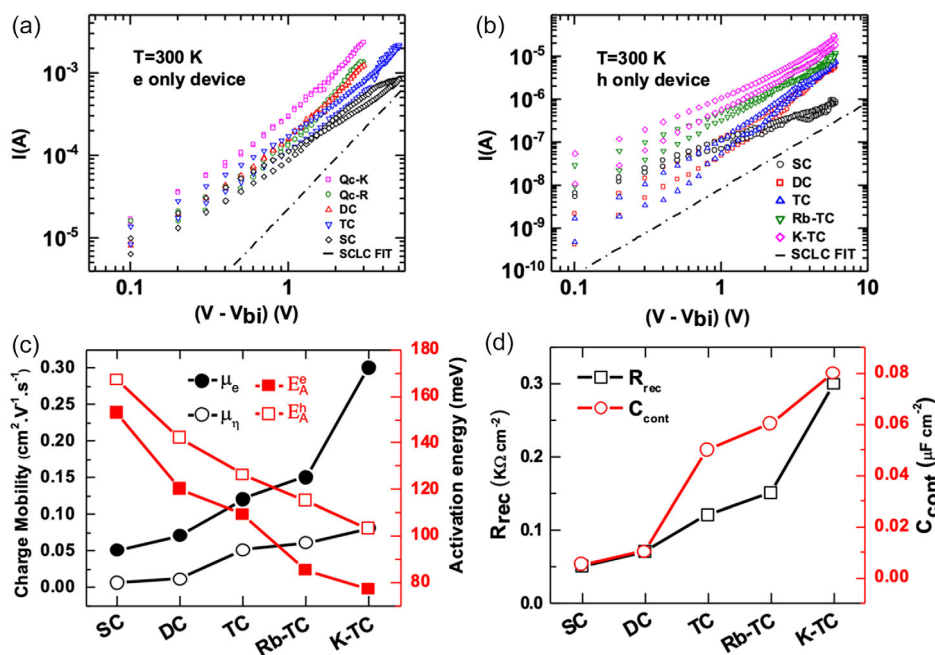


Figure 2. Charge transport behavior in alloyed perovskite devices. I - V characteristics of a) electron only devices (glass/FTO/ c -TiO₂ (≈ 50 nm)/mp-TiO₂ (≈ 200 nm)/perovskite (≈ 450 nm)/Al (≈ 80 nm)), b) hole only (glass/FTO/perovskite (≈ 550 nm)/Spiro-OMeTAD (≈ 200 nm)/Au (≈ 80 nm)) devices utilized for estimating the SCLC mobilities. In the x -axis, V is the applied voltage and V_{bi} is the built-in potential of the device. $(V - V_{bi})$ accounts for the effective energy barrier for electron/hole injection and collection. c) The trends in the extracted SCLC electron and hole mobilities and activation energies for perovskite solar cells with different perovskite compositions and passivation agents. d) The trends in the extracted recombination resistance (R_{rec}) and capacitance at the contacts (C_{cont}) from electrochemical impedance spectroscopy measurements for the abovementioned perovskites.

Supporting Information). The series RC circuit incorporates the dielectric relaxation capacitance (C_{dr}) and dielectric relaxation resistance (R_{dr}). In addition, the equivalent circuit also includes a parallel RC circuit, which corresponds to the recombination resistance (R_{rec}) and the capacitance at the contacts (C_{cont}) owing to the charge build-up at the perovskite and the adjacent contacts. In general, a higher magnitude of R_{rec} corresponds to lower possibility of loss of charge carriers due to recombination. Hence, correspondingly the J_{sc} increases. Contact capacitance we refer is capacitance realized at the contacts which would mean the capacitance expected when the solar cell is operated as a pure capacitive impedance. Under this circumstance if the thickness of different perovskite semiconductors is constant and the absorption coefficient and consequently the Q is constant, then the open-circuit voltage obtained would be directly proportional to the contact capacitance. This is what is observed in the impedance measurement and the effective voltage would be directly related to this parameter. Upon comparing the devices fabricated with perovskite films varying the A-site cation, we observe an increase in recombination resistance from $0.9 \text{ K}\Omega \cdot \text{cm}^{-2}$ for SC-based devices to $21.4 \text{ K}\Omega \cdot \text{cm}^{-2}$ for K-passivated TC perovskite (Figure 2d and S5a, Supporting Information). The observed increase in R_{rec} is consistent with the increase in the J_{sc} magnitude measured in photovoltaic cell. Similarly, the contact capacitance increases from $1.7 \mu\text{F} \cdot \text{cm}^{-2}$ for SC devices to $2.08 \mu\text{F} \cdot \text{cm}^{-2}$ for the K-passivated TC perovskite photovoltaic cell (Figure 2d) which matches the trend in V_{oc} observed for the solar cells. Notably, the passivated TC

shows the highest recombination resistance and C_{cont} and outperforms the other compositions. These results collectively show that K- and Rb-passivated TC possess superior optoelectronic and transport properties.

3. Conclusions

In summary, we systematically compared the optoelectronic and charge transport properties of mixed halide perovskites with varying cations (MA, FAMA, CsFAMA, K-passivated CsFAMA, Rb-passivated CsFAMA). Increasing cation complexity from SC, DC to TC significantly reduced the trap density in the thin film, as evidenced by a decrease in Urbach energy, an increase in PLQE, and improved charge carrier lifetime. This is also supported by the increase in charge carrier mobility and decreased activation energy for charge transport. Further passivation of the TC perovskite with K and Rb enhanced the optoelectronic characteristics of the semiconductor. The improvement in optoelectronic and charge transport properties for K- and Rb-passivated devices also resulted in relative enhancement in device efficiency by 15% and 13%, respectively, compared to reference devices.

4. Experimental Section

Film and Device Fabrication: All the organic cation salts were purchased from GreatCell Solar; the Pb compounds were from TCI and CsI and RbI from Alfa Aesar. Spiro-OMeTAD was purchased from Borun Chemicals

and used as received. Unless otherwise stated, all other materials were purchased from Sigma–Aldrich.

The SC perovskite MAPb(I_{0.85}Br_{0.15})₃ precursor was prepared by dissolving PbI₂ (1.2 M), MAI (1.11 M), MABr (0.21 M), and PbBr₂ (0.21 M) in a mixture of anhydrous DMF:DMSO (4:1, volume ratios). The DC-based perovskite (i.e., Cs_{0.06}FA_{0.79}MA_{0.15}Pb(I_{0.85}Br_{0.15})₃) was prepared by dissolving PbI₂ (1.2 M), FAI (1.11 M), MABr (0.21 M), and PbBr₂ (0.21 M) in a mixture of anhydrous DMF:DMSO (4:1, volume ratios). For TC perovskite precursor, this is followed by addition of 5 volume percent from CsI stock solution (1.5 M in DMSO) into the DC solution. Then, to make RB- and K-passivated TC perovskite, a 5 volume percent from RbI stock solution (1.5 M in DMF:DMSO, 4:1, volume ratios) and KI stock solution (1.5 M in DMF:DMSO, 4:1, volume ratios) was added to the above-mentioned TC solution, respectively. We then spin-coated the perovskite solutions using a two-step program at 2000 and 6000 rpm for 10 and 40 s, respectively, and dripping 150 μL of chlorobenzene after 30 s and annealed the spin-coated films at 100 °C for 1 h. All the film preparations were performed in a nitrogen-filled glove box. The devices were fabricated following the same procedures for substrate preparation as well as deposition of both electron and hole transport layers (i.e., TiO₂, Spiro-OMeTAD) as in our previous work.^[28]

PDS: PDS measurements were acquired on a custom-built setup by monitoring the deflection of a fixed wavelength (670 nm) laser probe beam following absorption of each monochromatic pump wavelength by a thin film immersed in an inert liquid FC-72 Fluorinert (3M Company). The Urbach energy (E_u) is calculated in each spectrum using the formula $a = a_0 e^{\frac{E}{E_u}}$, where a is the absorption coefficient, a_0 is a constant, and E is the photon energy.

TRPL: TRPL measurements were acquired with a gated intensified CCD camera system (Andor iStar DH740 CCI-010) connected to a grating spectrometer (Andor SR303i). Excitation was performed with femtosecond laser pulses which were generated in a homebuilt setup by second-harmonic generation (SHG) in a BBO crystal from the fundamental output (pulse energy 1.55 eV, pulse length 80 fs) of a Ti:Sapphire laser system (Spectra Physics Solstice). Temporal resolution of the PL emission was obtained by measuring the PL from the sample by stepping the iCCD gate delay relative to the pump pulse. The gate width was 20 ns. Carrier lifetime of each sample was obtained by fitting exponential decay function from the TRPL data.

SEM: The surface morphology of the films was examined using a ZEISS EVO LS 15 SEM. The accelerating voltage used is 15 kV using secondary electron.

XRD: XRD was performed using a Bruker X-ray D2 Phaser diffractometer with Cu K $\alpha_{1,2}$ radiation ($\lambda = 1.541 \text{ \AA}$). Spectra were collected with an angular range of $10 < 2\theta < 70$ and $\Delta\theta = 0.02173$ over 10 min. Measurements were made on as prepared films on glass.

GI-WAXS: GI-WAXS measurements were performed at the XMaS beamline (ESRF, France) as described in our previous works.^[15,29,30] A fixed-exit, water-cooled, double crystal Si(111) monochromator, placed at 25 m from the source was used to monochromatize the X-ray beam coming from a bending magnet ($E_c = 9.8 \text{ keV}$). The X-ray energy was tuned to 10 keV (1.2398 Å) and a Rh-coated toroidal mirror was used to focus the monochromatic beam horizontally and vertically. The beam flux was $\approx 5 \times 10^{10}$ photons s⁻¹ at the sample position. The original beam spot size was 500 (horizontal) \times 400 (vertical) μm^2 at the sample position. We employed a set of motorized slits (Huber, Germany) immediately before the sample to have a better-defined footprint in the vertical direction. The final beam spot size with slits was 300 (horizontal) \times 115 (vertical) μm^2 . The beam footprint was extended 300 μm horizontally and throughout the perovskite films. The samples were measured at an out-of-plane incident angle α_i of $\approx 0.3^\circ$, corresponding to a penetration depth of $\approx 140 \text{ nm}$, probing a significant portion of the bulk. Data processing was performed with the MATLAB Software (GI-WAXS GUI) described in our previous works.^[31,32]

Solar Cell Characterization: Current–voltage characteristics were recorded by applying an external potential bias to the cell while recording the generated photocurrent with a digital source meter (Keithley Model 2400). The light source was a 450 W xenon lamp (Oriol) equipped with a Schott-K113 Tempax sunlight filter (Prazisions Glas & Optik GmbH)

to match the emission spectrum of the lamp to the AM1.5G standard. Before each measurement, the exact light intensity was determined using a calibrated Si reference diode equipped with an infrared cutoff filter (KG-3, Schott). EQE spectra were recorded as a function of wavelength under a constant white light bias of approximately 5 mW cm⁻² supplied by an array of white light emitting diodes. The excitation beam coming from a 300 W xenon lamp (ILCTechnology) was focused through a Gemini-180 double monochromator (Jobin Yvon Ltd.) and chopped at approximately 2 Hz. The signal was recorded using a Model SR830 DSP Lock-In Amplifier (Stanford Research Systems). All measurements were conducted using a nonreflective metal aperture of 0.105 cm² to define the active area of the device and avoid light scattering through the sides.

Bulk Transport Measurements: Hole only devices were fabricated on precleaned FTO substrates (15 $\Omega \text{ sq}^{-1}$). The mesoporous perovskite layer with the different interfacial layers was fabricated in the same way as described for the solar cell device fabrication. Metal electrodes Au for the devices were coated by thermal evaporation (10⁻⁶ mbar, 0.1 Å s⁻¹, 80 nm thick). The devices were characterized using Keithley 4200 SCS and temperature was varied using a RF probe station from Cryogenic Technologies.

EIS: EIS of the solar cells was carried out using a precision impedance analyzer HP4294A while the device was illuminated using a home built light source with close to 1 Sun intensity. The device was driven by a small AC frequency of 30 mV and obtained impedance parameters were fitted with a standard circuit to estimate the physical parameters. In the EIS measurements, the device is driven at a small AC voltage of 30 mV while the frequency is swept from 100 Hz to 10 MHz. The equivalent circuit for impedance spectroscopy measurement was reported in previous literature^[33] and is shown in Figure S5b, Supporting Information.

Supporting Information

Supporting Information is available from the Wiley Online Library or from the author.

Acknowledgements

Q.L. is grateful for the support from the Chinese Scholarship Council (CSC) and the Faculty of Mathematical & Physical Sciences (MAPS) at University College London (UCL). M.A.-J. acknowledges the Royal Society (RGS\R1\211068) and Cambridge Materials Limited for their funding and technical support. M.A.-J. acknowledges the Department for Energy Security and Net Zero (Project ID: NEXTCCUS), University College London's Research, Innovation and Global Engagement, and University of Sydney–University College London Partnership Collaboration Awards for their financial support. M.A.-J. acknowledges the ACT program (Accelerating CCS Technologies, Horizon2020 Project No. 691712) for the financial support of the NEXTCCUS project (project ID: 327327). S.P.S. acknowledges funding from DAE and SERB (SRG/2022/000162, SERB-SRG/2020/001641), Government of India and Royal Society through Newton Alumni Fellowship. XMaS is a UK national research facility supported by EPSRC. M.A. and S.L. are grateful to all the beamline team staff for their support, in particular to Dr Oier Binkondoa for facilitating remote GI-WAXS measurements.

Conflicts of Interest

The authors declare no conflict of interest.

Data Availability Statement

The data that support the findings of this study are available from the corresponding author upon reasonable request.

Keywords

charge transport properties, electrochemical impedance spectroscopy, mixed cation perovskites, perovskite solar cells

Received: March 31, 2023

Revised: May 19, 2023

Published online:

- [1] NREL Best Research-Cell Efficiency Chart, <https://www.nrel.gov/pv/cell-efficiency.html>, (accessed: March 2023).
- [2] W. Zhang, G. E. Eperon, H. J. Snaith, *Nat Energy* **2016**, *1*, 16048.
- [3] Q. Chang, D. Bao, B. Chen, H. Hu, X. Chen, H. Sun, Y. M. Lam, J. X. Zhu, D. Zhao, E. E. M. Chia, *Commun. Phys.* **2022**, *5*, 187.
- [4] R. J. Sutton, G. E. Eperon, L. Miranda, E. S. Parrott, B. A. Kamino, J. B. Patel, M. T. Hörlantner, M. B. Johnston, A. A. Haghighirad, D. T. Moore, H. J. Snaith, *Adv. Energy Mater.* **2016**, *6*, 1502458.
- [5] N. Yaghoobi Nia, M. Zendehehdel, L. Cinà, F. Matteocci, A. di Carlo, *J. Mater. Chem. A Mater.* **2018**, *6*, 659.
- [6] A. Kojima, K. Teshima, Y. Shirai, T. Miyasaka, *J. Am. Chem. Soc.* **2009**, *131*, 6050.
- [7] A. Y. Alsalloum, B. Turedi, X. Zheng, S. Mitra, A. A. Zhumekenov, K. J. Lee, P. Maity, I. Gereige, A. AlSaggaf, I. S. Roqan, O. F. Mohammed, O. M. Bakr, *ACS Energy Lett.* **2020**, *5*, 657.
- [8] C. H. Chiang, C. G. Wu, *ACS Nano* **2018**, *12*, 10355.
- [9] K. Wang, Z. Jin, L. Liang, H. Bian, D. Bai, H. Wang, J. Zhang, Q. Wang, L. Shengzhong, *Nat. Commun.* **2018**, *9*, 4544.
- [10] N. Pellet, P. Gao, G. Gregori, T. Y. Yang, M. K. Nazeeruddin, J. Maier, M. Grätzel, *Angew. Chem. Int. Ed.* **2014**, *53*, 3151.
- [11] N. J. Jeon, J. H. Noh, W. S. Yang, Y. C. Kim, S. Ryu, J. Seo, S. Il Seok, *Nature* **2015**, *517*, 476.
- [12] M. Saliba, T. Matsui, J. Y. Seo, K. Domanski, J. P. Correa-Baena, M. K. Nazeeruddin, S. M. Zakeeruddin, W. Tress, A. Abate, A. Hagfeldt, M. Grätzel, *Energy Environ. Sci.* **2016**, *9*, 1989.
- [13] J. Peng, D. Walter, Y. Ren, M. Tebyetekewa, Y. Wu, T. Duong, Q. Lin, J. Li, T. Lu, M. A. Mahmud, O. L. C. Lem, S. Zhao, W. Liu, Y. Liu, H. Shen, L. Li, F. Kremer, H. T. Nguyen, D. Y. Choi, K. J. Weber, K. R. Catchpole, T. P. White, *Science* **2021**, *371*, 390.
- [14] M. Saliba, T. Matsui, K. Domanski, J. Y. Seo, A. Ummadisingu, S. M. Zakeeruddin, J. P. Correa-Baena, W. R. Tress, A. Abate, A. Hagfeldt, M. Grätzel, *Science* **2016**, *354*, 206.
- [15] M. Abdi-Jalebi, Z. Andaji-Garmaroudi, S. Cacovich, C. Stavrakas, B. Philippe, J. M. Richter, M. Alsari, E. P. Booker, E. M. Hutter, A. J. Pearson, S. Lilliu, T. J. Savenije, H. Rensmo, G. Divitini, C. Ducati, R. H. Friend, S. D. Stranks, *Nature* **2018**, *555*, 497.
- [16] S. Feldmann, S. Macpherson, S. P. Senanayak, M. Abdi-Jalebi, J. P. H. Rivett, G. Nan, G. D. Tainter, T. A. S. Doherty, K. Frohna, E. Ringe, R. H. Friend, H. Sirringhaus, M. Saliba, D. Beljonne, S. D. Stranks, F. Deschler, *Nat. Photonics* **2020**, *14*, 123.
- [17] T. Jesper Jacobsson, J. P. Correa-Baena, M. Pazoki, M. Saliba, K. Schenk, M. Grätzel, A. Hagfeldt, *Energy Environ. Sci.* **2016**, *9*, 1706.
- [18] D. W. Ferdani, S. R. Pering, D. Ghosh, P. Kubiak, A. B. Walker, S. E. Lewis, A. L. Johnson, P. J. Baker, M. S. Islam, P. J. Cameron, *Energy Environ. Sci.* **2019**, *12*, 2264.
- [19] M. Abdi-Jalebi, Z. Andaji-Garmaroudi, A. J. Pearson, G. Divitini, S. Cacovich, B. Philippe, H. Rensmo, C. Ducati, R. H. Friend, S. D. Stranks, *ACS Energy Lett.* **2018**, *3*, 2671.
- [20] J. C. Brauer, D. Tsokkou, S. Sanchez, N. Droseros, B. Roose, E. Mosconi, X. Hua, M. Stolterfoht, D. Neher, U. Steiner, F. De Angelis, A. Abate, N. Banerji, *J. Chem. Phys.* **2020**, *152*, 104703.
- [21] S. Tan, I. Yavuz, N. De Marco, T. Huang, S. J. Lee, C. S. Choi, M. Wang, S. Nuryeva, R. Wang, Y. Zhao, H. C. Wang, T. H. Han, B. Dunn, Y. Huang, J. W. Lee, Y. Yang, *Adv. Mater.* **2020**, *32*, 1906995.
- [22] R. Imani, C. H. Borca, M. Pazoki, T. Edvinsson, *RSC Adv.* **2022**, *12*, 25415.
- [23] J. M. Richter, M. Abdi-Jalebi, A. Sadhanala, M. Tabachnyk, J. P. H. Rivett, L. M. Pazos-Outón, K. C. Gödel, M. Price, F. Deschler, R. H. Friend, *Nat. Commun.* **2016**, *7*, 13941.
- [24] H.-S. Kim, A. Hagfeldt, N.-G. Park, *Chem. Commun.* **2019**, *55*, 1192.
- [25] M. Stolterfoht, M. Grischek, P. Caprioglio, C. M. Wolff, E. Gutierrez-Partida, F. Peña-Camargo, D. Rothhardt, S. Zhang, M. Raoufi, J. Wolansky, M. Abdi-Jalebi, S. D. Stranks, S. Albrecht, T. Kirchartz, D. Neher, M. Stolterfoht, M. Grischek, P. Caprioglio, C. M. Wolff, E. Gutierrez-Partida, F. Peña-Camargo, D. Rothhardt, S. Zhang, M. Raoufi, J. Wolansky, D. Neher, S. Albrecht, M. Abdi-Jalebi, S. D. Stranks, T. Kirchartz, *Adv. Mater.* **2020**, *32*, 2000080.
- [26] D. J. Kubicki, D. Prochowicz, A. Hofstetter, S. M. Zakeeruddin, M. Grätzel, L. Emsley, *J. Am. Chem. Soc.* **2017**, *139*, 14173.
- [27] M. I. Saidaminov, K. Williams, M. Wei, A. Johnston, R. Quintero-Bermudez, M. Vafaie, J. M. Pina, A. H. Proppe, Y. Hou, G. Walters, S. O. Kelley, W. A. Tisdale, E. H. Sargent, *Nat. Mater.* **2020**, *19*, 412.
- [28] M. Abdi-Jalebi, M. I. Dar, A. Sadhanala, S. P. Senanayak, F. Giordano, S. M. Zakeeruddin, M. Grätzel, R. H. Friend, *J. Phys. Chem. Lett.* **2016**, *7*, 3264.
- [29] B. Zhao, S. Bai, V. Kim, R. Lamboll, R. Shivanna, F. Auras, J. M. Richter, L. Yang, L. Dai, M. Alsari, X. J. She, L. Liang, J. Zhang, S. Lilliu, P. Gao, H. J. Snaith, J. Wang, N. C. Greenham, R. H. Friend, D. Di, *Nat. Photonics* **2018**, *12*, 783.
- [30] M. Alsari, O. Bikondoa, J. Bishop, M. Abdi-Jalebi, L. Y. Ozer, M. Hampton, P. Thompson, M. T. Hörlantner, S. Mahesh, C. Greenland, J. E. Macdonald, G. Palmisano, H. J. Snaith, D. G. Lidzey, S. D. Stranks, R. H. Friend, S. Lilliu, *Energy Environ. Sci.* **2018**, *11*, 383.
- [31] S. Lilliu, M. Alsari, O. Bikondoa, J. E. Macdonald, M. S. Dahlem, *Sci. Rep.* **2015**, *5*, 10633.
- [32] S. Lilliu, J. Griffin, A. T. Barrows, M. Alsari, B. Curzadd, T. G. Dane, O. Bikondoa, J. E. Macdonald, D. G. Lidzey, *CrystEngComm* **2016**, *18*, 5448.
- [33] M. Abdi-Jalebi, M. I. Dar, S. P. Senanayak, A. Sadhanala, Z. Andaji-Garmaroudi, L. M. Pazos-Outón, J. M. Richter, A. J. Pearson, H. Sirringhaus, M. Grätzel, R. H. Friend, *Sci. Adv.* **2019**, *5*, eaav2012.